

Vegetation profiles in tropical forests from multibaseline interferometric synthetic aperture radar, field, and lidar measurements

R. N. Treuhaft,¹ B. D. Chapman,² J. R. dos Santos,³ F. G. Gonçalves,⁴ L. V. Dutra,⁵ P. M. L. A. Graça,⁶ and J. B. Drake⁷

Received 9 December 2008; revised 21 May 2009; accepted 25 August 2009; published 15 December 2009.

[1] This paper addresses the estimation of vertical vegetation density profiles from multibaseline interferometric synthetic aperture radar (InSAR) data from the AirSAR aircraft at C band over primary, secondary, and abandoned-pasture stands at La Selva Biological Station, Costa Rica in 2004. Profiles were also estimated from field data taken in 2006 and lidar data taken with the LVIS, 25 m spot instrument in 2005. After motivating the study of tropical forest profiles based on their role in the global carbon cycle, ecosystem state, and biodiversity, this paper describes the InSAR, field, and lidar data acquisitions and analyses. Beyond qualitative agreement between profiles from the 3 measurement techniques, results show that InSAR and lidar profile-averaged mean height have RMS scatters about field-measured means of 3.4 m and 3.2 m, 16% and 15% of the average mean height, respectively. InSAR and lidar standard deviations of the vegetation distribution have RMS scatters about the field standard deviations of 1.9 m and 1.5 m, or 27% and 21%, respectively. Dominant errors in the profile-averaged mean height for each measurement technique were modeled. InSAR inaccuracies, dominated by ambiguities in finding the ground altitude and coherence calibration, together account for about 3 m of InSAR error in the mean height. The dominant, modeled error for the field measurements was the inaccuracy in modeling the trees as uniformly filled volumes of leaf area, inducing field errors in mean height of about 3 m. The dominant, modeled lidar error, also due to finding the ground, was 2 m.

Citation: Treuhaft, R. N., B. D. Chapman, J. R. dos Santos, F. G. Gonçalves, L. V. Dutra, P. M. L. A. Graça, and J. B. Drake (2009), Vegetation profiles in tropical forests from multibaseline interferometric synthetic aperture radar, field, and lidar measurements, *J. Geophys. Res.*, 114, D23110, doi:10.1029/2008JD011674.

1. Introduction

[2] Forests cover 40% of the Earth's solid, ice-free surface [Waring and Running, 1989]. Tropical rain forests contain 40% of the Earth's forested biomass, and tropical seasonal forests contain another 15% [Schlesinger, 1991; Saugier *et al.*, 2001]. Global measurements of the 3-dimensional structure of forests bear on the assessment of their role in the global carbon cycle. Global monitoring also contributes

to the understanding of ecosystem state and biodiversity. Traditional remote sensing of the Earth primarily registers terrestrial features in the two lateral directions—latitude and longitude—along the Earth's surface. The relatively new 3-dimensional remote sensing techniques of interferometric synthetic aperture radar (InSAR) [Treuhaft *et al.*, 2004] and lidar [Lefsky *et al.*, 2002] can register forest features explicitly in the third, vertical dimension. Due to their high vegetation density and 3-dimensional complexity, tropical forests represent a special challenge for these new techniques, as well as for field measurements.

[3] This paper presents vertical profiles of forest vegetation estimated from InSAR data over tropical forests at the La Selva Biological Station in Costa Rica in March 2004. The main purpose of the paper is to investigate the relationship between those InSAR profiles to profiles estimated from field measurements in February 2006 and those estimated from lidar taken in March 2005, and to compare the levels of agreement between profiles to proposed error models for each technique. The next subsection discusses the need for vegetation profiles in various disciplines of global ecology. Section 2 describes the La Selva site and the stands measured. It also describes the InSAR and field

¹Tracking Systems and Applications, Jet Propulsion Laboratory, California Institute of Technology, Pasadena, California, USA.

²Radar Science and Engineering, Jet Propulsion Laboratory, California Institute of Technology, Pasadena, California, USA.

³Divisão de Sensoriamento Remoto, Instituto Nacional de Pesquisas Espaciais, São José dos Campos, Brazil.

⁴Department of Forest Ecosystems and Society, Oregon State University, Corvallis, Oregon, USA.

⁵Divisão de Processamento de Imagens, Instituto Nacional de Pesquisas Espaciais, São José dos Campos, Brazil.

⁶Departamento de Ecologia, Instituto Nacional de Pesquisas da Amazônia, Manaus, Brazil.

⁷Forest Service, USDA, Tallahassee, Florida, USA.

measurement techniques performed by the authors. The lidar data acquired by the LVIS system [Blair *et al.*, 1999] will also be described. Section 3 shows a sample of profile results and profile moments of the three measurement approaches, while section 4 models dominant errors in the InSAR, field, and lidar measurements. Section 5 contains conclusions.

1.1. Ecological Importance of Vegetation Profiles

[4] The structure of forests, particularly in the vertical direction, has been used as an indicator of aboveground biomass, ecosystem state, and biodiversity. The distribution of aboveground biomass in turn is key to understanding the global carbon cycle [Houghton, 2005]. Before the InSAR and lidar techniques, microwave based methods showed the most robust correlations with forest biomass and have been used to estimate biomass for a variety of forest types [e.g., Dobson *et al.*, 1992; Moghaddam *et al.*, 1994; Imhoff, 1995; Luckman *et al.*, 1998; dos Santos *et al.*, 2003; Le Toan *et al.*, 2004; Lucas *et al.*, 2006; Saatchi *et al.*, 2007]. The above references used some combination of radar power from various polarizations and polarimetric phase to estimate biomass. Generally, the higher the power, the higher the biomass. However, almost all of these studies show a saturation effect above 50–180 Mg/hectare (ha), depending on the radar wavelength, the type of forest, and instrumental parameters. In the neighborhood of and beyond these saturation points, incrementally higher biomasses typical of tropical forests no longer have a discernable effect on the radar power, making biomass estimation from radar power inaccurate or impossible. Saturation with optical remote sensing [e.g., Steininger, 2000] has also been observed. In contrast, the most accurate high-biomass measurements to date from remote sensing include vertical structure. Some studies involving InSAR [Neeff *et al.*, 2005] and lidar [Lefsky *et al.*, 2005] have used remotely sensed forest height, sometimes coupled with other observations, and have achieved estimates of biomass beyond 200 Mg/ha without saturation. Others have used functions of the profile, such as the lidar-derived height of median energy [Drake *et al.*, 2002a] or moments of the profile such as InSAR-derived mean or standard deviation of the vertical profile [Treuhaft *et al.*, 2003]. Treuhaft *et al.* [2003] and Neeff *et al.* [2005] combined structural information with hyperspectral and radar power respectively.

[5] Vertical structure information also applies to the characterization of the state of the forest ecosystem, such as fire susceptibility or fire history, and regional or local climate change. The vapor pressure deficit [Ray *et al.*, 2005], for example, was found to be strongly correlated with fire-spread rate. Canopy leaf area index and canopy height were in turn found to correlate with vapor pressure deficit. Various other profile metrics have been correlated with understorey biomass, which is a key factor in the spread of ground fires to the canopy [Skowronski *et al.*, 2007]. Vertical structure information has also been used to characterize fire dynamics with fuel models [Mutlu *et al.*, 2008]. In tropical rain forests, forest fires can cause significant release of carbon dioxide to the atmosphere, in extreme cases of the same order of magnitude as global fossil fuel emissions [Cochrane, 2003]. The remote sensing of fire susceptibility is potentially an important monitor of

one of the factors affecting the atmospheric global carbon balance and climate. Because earlier fires predispose areas to subsequent fires [Cochrane and Schulze, 2003], the structural signatures of burned areas derived from vertical profiles could potentially be used as indicators of consequent fire susceptibility. Vertical structural features have a strong effect on the exchange of water and energy with the atmosphere and thus can affect regional or local climate. For example, a model exercise determined that replacing the tropical forests of the Amazon basin with pasture would decrease evapotranspiration and increase albedo [Shukla *et al.*, 1990]. In turn, the regional surface temperature would rise by 1–3°C, and the precipitation would decrease by several hundred mm/year. At the stand, “microclimate” level, for Douglas fir sites in western Washington, few °C changes in temperature at 2 m above the ground surface were correlated with clear cutting and selective logging [Chen *et al.*, 1999]. Microclimate edge effects on soil moisture and evapotranspiration, signaled by abrupt changes in vegetation structure, have also been measured in Amazonian forests [e.g., Camargo and Kapos, 1995]. Remotely sensing changes in the vertical structure of forests due to clear cutting or selective logging could enable the monitoring of changes in regional climate or microclimate.

[6] Biodiversity has also been shown to depend on structural characteristics of the forest. For example, MacArthur and MacArthur [1961] found a strong correlation between bird species diversity (BSD) and an entropy-like function of a leaf area density vertical profile determined by direct field measurement, forest height diversity (FHD). The diversity function for both BSD and FHD was defined as

$$\text{BSD, FHD} = \sum_i -p_i \ln p_i \quad (1)$$

where p_i is the fraction of birds that belong to species i for BSD, and it is the fraction of foliage area within height bin i for FHD. A wide range of vertical resolutions was used—between 6 inches and 15 feet. It should be noted that the numerical value of FHD for foliage diversity depends on bin widths, but presumably the qualitative correlation between BSD and FHD observed by MacArthur and MacArthur persists for different choices of vertical bin size. Subsequent studies have found a wide range of correlation between BSD and FHD as in (1) [Wiens, 1989]. Polarimetric radar power has also been correlated with bird species diversity [Imhoff *et al.*, 1997], but that study suggested direct structural measurements of the type available from InSAR and lidar would be an improvement over simple radar power. Turner *et al.* [2003] review spectral and structural possibilities for remote sensing of terrain characteristics affecting species diversity, including vertical canopy profiles. Weak correlations between species health and vegetation height have also been observed [Bradbury *et al.*, 2005].

1.2. Fundamental Limitations of InSAR in Measuring Vegetation Profiles

[7] Beyond characterizing biomass, ecosystem state, and biodiversity, another reason to study vegetation profiles with InSAR in particular is to probe its fundamental limitations in measuring the vertical structure of forests.

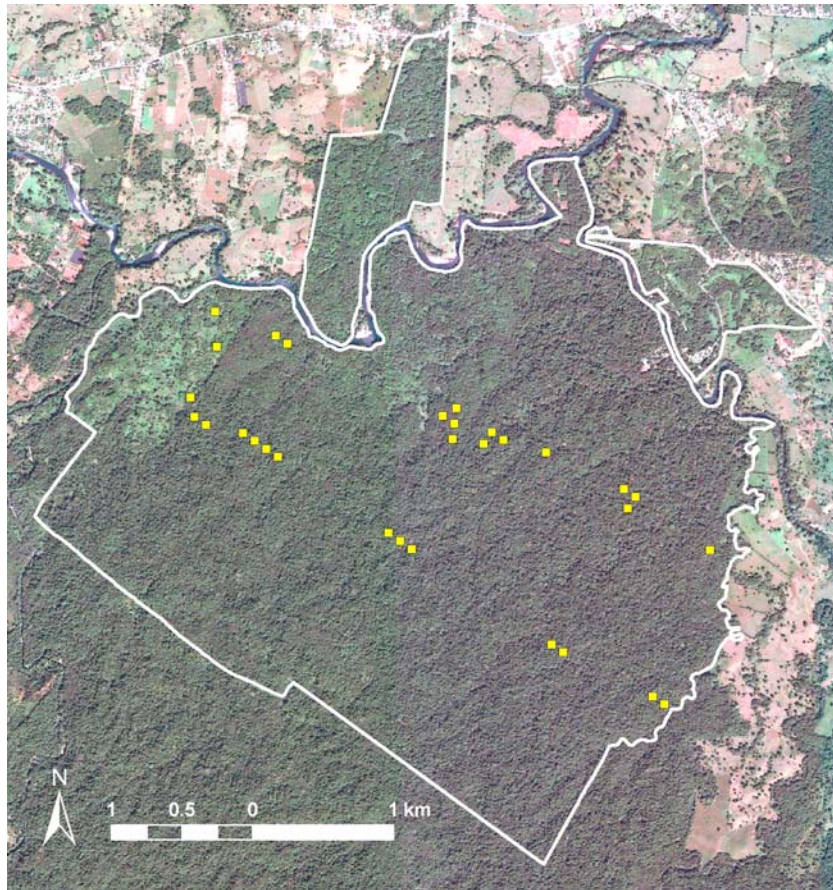


Figure 1. QuickBird image of La Selva Biological Station in Costa Rica, outlined in white. The yellow squares are the locations of the 30 stands used in this paper, which were placed at an incidence angle of $\approx 35^\circ$ to the flight lines of AirSAR over La Selva in 2004. Center of image is approximately 10.421864° latitude and -84.021195° longitude. Figure reprinted with permission from the La Selva Biological Station.

Although multibaseline interferometry has been used in astronomy to measure stellar structure for the last 80 years [Thompson *et al.*, 1986], interferometry applied to forests must be tested for instrumental limitations and its ability to measure structure along the direction of signal attenuation. While the vertical profile resolution from InSAR with a modest number of baselines is generally worse than that of lidar, InSAR's coverage is 4 orders of magnitude broader [Treuhaft *et al.*, 2004] and therefore lends itself to global monitoring. Part of the reason for InSAR's improved coverage is simply due to the fact that sensors with longer wavelengths (microwave wavelength \approx few cm, optical wavelength $\approx 10^{-4}$ cm) have wider beams, and hence cover more terrain. Another reason for the improved coverage of InSAR is the technique's ability to see through clouds. This is especially important for tropical forests. In the Amazon Basin, for example, with a repeat time of 16 days, the chances of obtaining remote sensing data with 50% or less cloud cover in a month is often less than 30% [Asner, 2001].

[8] Estimation of profiles from multibaseline InSAR is relatively new, with the first demonstration of profile sensitivity by Reigber and Moreira [2000]. InSAR-based profiles of leaf area density were estimated in Central Oregon [Treuhaft *et al.*, 2002]. The current work is the first

to attempt InSAR profiles in tropical forests, although Hajnsek *et al.* [2009] estimated tropical forest heights with 2 m accuracy by assuming uniform profiles at L band.

2. Site and Remote Sensing Measurements

2.1. Site Characteristics and Radar Flights

[9] La Selva is a tropical wet forest [Holdridge, 1947] and is characterized by a high diversity of trees, lianas, and epiphytes [McDade *et al.*, 1994]. It is comprised of about 55% primary forest. It gets about 4 m/year of rainfall. 30 sites of dimensions $50 \text{ m} \times 50 \text{ m}$ were chosen as remote sensing study targets. Of those, 20 were primary forests—6 of which were selectively logged—7 were secondary forests, and 3 were abandoned pastures. The sites were chosen along two flight lines of the AirSAR aircraft carrying the radar [Van Zyl *et al.*, 1997] used for the InSAR measurements, as indicated by yellow squares in Figure 1. For the northern line, the plane carrying the radar flew from southeast to northwest at a heading of 296 degrees. For the southern line, the plane flew from northwest to southeast at a heading of 124 degrees. Because AirSAR has only two physical baselines, the so-called “bistatic” of 2.5 m and “ping-pong” of 5 m, and because many more were needed to estimate profiles, the aircraft was flown at 7 altitudes over La Selva,

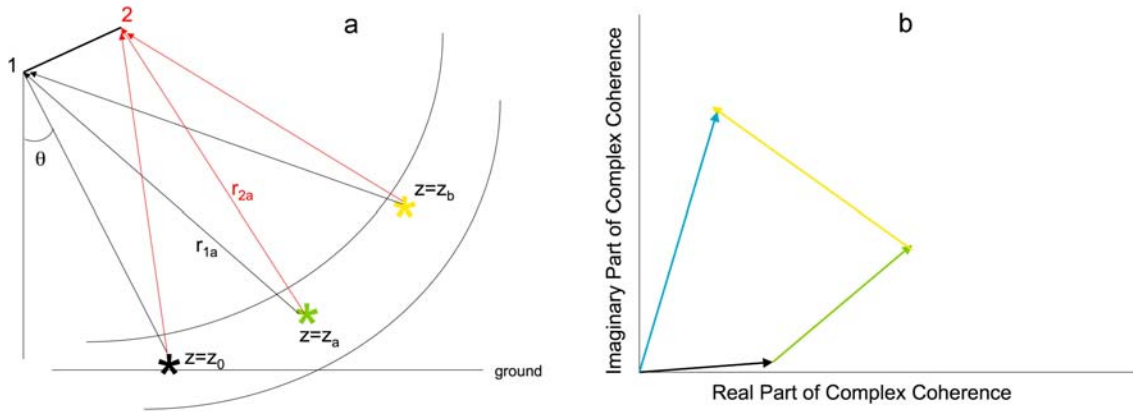


Figure 2. (a) The contribution to the InSAR complex coherence of the ground return at $z = z_0$, and two vegetation elements at heights z_a and z_b . The curved lines depict the ranges allowed by the radar. The interferometric phase for each element is the difference between the path lengths of the black and red lines for that element, in units of the wavelength, multiplied by 2π . This differential distance for each element is in turn proportional to its height above the surface. The path lengths from scatterer a to the “1” and “2” ends of the baselines are indicated by r_{1a} and r_{2a} . (b) The angles of the component vectors with the x axis are proportional to the InSAR phases of each, and to the heights z_0 , z_a , and z_b . The lengths of the components are proportional to the total vegetation signal at each altitude. The coherence of the net InSAR observations is the length of the blue vector divided by the sum of the lengths of the others. The phase of the net observation is the angle of the blue vector with the x axis.

ranging from 1278 m to 8062 m along the tracks in Figure 1. By flying the two fixed baselines at many altitudes, the equivalent of up to 14 baselines was produced (see (3) and the discussion of the α_z parameter). All forest stands for all altitudes were maintained at close to 35° incidence angle, with the incidence angle of some of the stands for the lowest altitudes deviating from 35° by $\pm 5^\circ$. AirSAR took fixed baseline, vertical polarization InSAR measurements at C band (wavelength 5.6 cm) and L band (wavelength 24 cm), but only the C band results will be discussed in this paper. AirSAR also took repeat pass, fully polarimetric InSAR measurements—where the baseline is synthesized by two different passes over the same terrain—at L and P band (wavelength 80 cm); the analyses of these data are underway, but are not part of this paper. The InSAR, field, and lidar measurements at La Selva are described below.

2.2. InSAR Profiles: General Description

[10] The InSAR measurement is called the “complex coherence”. It consists of an amplitude, called the “coherence,” and a phase, which were broadly characterized in terms of vegetation characteristics by *Treuhaft et al.* [2004]. More detailed descriptions of the relationship between the complex coherence and vegetation structural parameters are given by *Rodriguez and Martin* [1992], *Treuhaft et al.* [1996], *Cloude and Papathanassiou* [1998], *Treuhaft and Siqueira* [2000], and *Sarabandi and Lin* [2000]. A technical approach to the complex coherence when combined with lidar structure is given by *Slatton et al.* [2001]. Following is a description of the complex coherence on the vertical characteristics of the vegetation distribution only. The dependence of InSAR on signal-to-noise and target range and azimuth characteristics are treated in the references above.

[11] Figure 2 schematically shows the InSAR complex coherence due to returns from the ground and two vegeta-

tion elements at heights z_a and z_b , within the radar range resolution, indicated by the region within the curved lines. The vegetation elements, referred to as “scatterers,” can be leaves, branches, twigs, or trunks, all of which return a signal to the radar. In a complete statistical formulation of InSAR [e.g., *Treuhaft et al.*, 1996], a “scatterer” is really a statistical combination of all of the above types of forest elements, but this level of formal detail will not be pursued here. The InSAR phase at any altitude is the difference in path length from a scatterer to the “1” and “2” ends of the baseline—the difference between the length of the black and red lines—expressed in units of the wavelength and multiplied by 2π . For the scatterer at z_a in Figure 2a,

$$\text{InSAR Phase} \equiv \phi_a = \frac{2\pi}{\lambda}(r_{1a} - r_{2a}) \quad (2)$$

where r_{1a} and r_{2a} are the path lengths from scatterer a to the “1” and “2” ends of the baseline, respectively, and λ is the observing wavelength—this definition of phase assumes there is one transmitter at one end of the baseline and a receiver at each end. The path length difference and consequent phase is higher for the vegetation at z_b than for that at z_a or the ground altitude. It is shown by *Treuhaft et al.* [1996], for example, that the InSAR phase, ϕ_a , can be expressed for the vegetation element at altitude z_a as

$$\phi_a = \phi_0 + \left. \frac{\partial \phi}{\partial z} \right|_{z=z_0} (z_a - z_0) \equiv \phi_0 + \alpha_z (z_a - z_0) \quad (3)$$

where z_0 and ϕ_0 are the altitude and phase of the ground surface. The partial derivative of phase with respect to altitude, α_z , is defined by (3). It is taken holding the range and azimuth coordinates constant. This derivative is proportional to the baseline length B , and inversely

proportional to λ and the height of the radar H . For the physical baselines and aircraft altitudes mentioned above, α_z 's in this experiment ranged from 0.043 m^{-1} to 0.54 m^{-1} . For forest vegetation, and for a single α_z , returns such as those in Figure 2a will add together vectorially as in Figure 2b to form the total InSAR observation, the complex coherence. In Figure 2b, the phase of each vector is proportional to the altitude of each vegetation component above the ground, as in (3), and is plotted as the angle between the vector and the x axis. The length of each vector is proportional to the radar signal returned from that altitude. The radar signal in turn is proportional to the backscattering strength per vegetation element and the number density of vegetation elements, the product of which, we argue below, can be considered proportional to leaf area density. The vector length is also inversely proportional to the level of attenuation at that altitude. The phase of the net InSAR observation due to the ground and two vegetation elements is the phase of the blue vector. The length of the blue vector divided by the sum of the lengths of the others is the coherence of the net InSAR observation. Note that, generally, the more vertically extended the vegetation, the higher the phase of the net InSAR observation, and the lower the coherence. For the many vegetation elements in a real forest, the vector addition describing the complex coherence in Figure 2b becomes an integral as in (4) [Treuhaft *et al.*, 1996]:

$$\begin{aligned} \text{Complex Coherence} &= \frac{e^{i\phi_0} \mathcal{F}(\alpha_z)}{\mathcal{F}(0)} \text{ where} \\ \mathcal{F}(\alpha_z) &\equiv \int_0^{h_v} dz e^{i\alpha_z z} N(z) \langle f_b^2(z) \rangle \\ &\times \exp - \left[\frac{4\lambda}{\cos \theta} \int_z^{h_v} \langle \text{Im}(f_f(z')) \rangle N(z') dz' \right] \end{aligned} \quad (4)$$

where h_v is the height of the tallest vegetation. The first line in the definition of $\mathcal{F}(\alpha_z)$ describes the strength of the total signal sent by the scatterers back to the radar. This strength depends on $N(z)$ the number density of scatterers per unit volume in the scene and $\langle f_b^2(z) \rangle$ the average squared backscattering amplitude per scatterer at altitude z [Ishimaru, 1978]. The exponential in the second line of (4) describes the attenuation of signals as they travel to or from the top of the canopy to any point z in the canopy, with the average imaginary part of the forward scattering amplitude, $\langle \text{Im}(f_f(z)) \rangle$, describing the average attenuation per scatterer at location z .

[12] In order to estimate and evaluate profiles from InSAR data, (4) must be related to a vegetation density, which can be estimated from InSAR data and compared to field-measured profiles. At C band ($\lambda = 5.6 \text{ cm}$), it is reasonable to assume most scatterers are leaves. The scattering amplitudes, f_b and f_f in (4), are proportional to the area of the scatterer, for a thin scatterer like a leaf. Thus it could be argued that $\langle \text{Im}(f_f(z)) \rangle N(z)$ is proportional to the leaf area density (LAD), which is the one-sided leaf area per unit volume [Asrar *et al.*, 1989]. The $\langle f_b^2(z) \rangle$ term, however, is proportional to the area squared. Denoting $Rel(z)$ as the relative LAD with peak normalized to unity, $\mathcal{F}(\alpha_z)$ in (4) could then be written in terms of relative LAD as (apart

from constants which will cancel in forming the complex coherence of (4))

$$\begin{aligned} \mathcal{F}(\alpha_z) &= \int_0^{h_v} dz e^{i\alpha_z z} Rel(z) \sqrt{\langle f_b^2(z) \rangle} \\ &\times \exp - \left[\frac{2\sigma_x}{\cos \theta} \int_z^{h_v} Rel(z') dz' \right] \end{aligned} \quad (5)$$

where σ_x is identified as the peak profile extinction coefficient if $Rel(z)$ is normalized with a peak value of "1". In (5), two profiles appear, the relative leaf area density and the square root of the squared backscattering amplitude. We will make the assumption that $\langle f_b^2(z) \rangle$ is independent of z , and can therefore be factored out of the integral and cancels with the denominator $\mathcal{F}(0)$ in (4). This assumption is equivalent to saying that the nature of the ensemble of scatterers, for example the histogram of leaf areas at any altitude, does not change from the bottom to the top to the canopy. The only thing that is changing is $N(z)$, the number density of scatterers. This assumption establishes the dependence of InSAR on vegetation density parameters used to estimate leaf area density profiles

$$\begin{aligned} \text{Complex Coherence} &= \frac{e^{i\phi_0} \mathcal{F}(\alpha_z)}{\mathcal{F}(0)} \text{ where} \\ \mathcal{F}(\alpha_z) &\approx \int_0^{h_v} dz e^{i\alpha_z z} Rel(z) \times \exp - \left[\frac{2\sigma_x}{\cos \theta} \int_z^{h_v} Rel(z') dz' \right] \end{aligned} \quad (6)$$

[13] While visual observations of the apparent diversity in leaf areas at any altitude in a tropical forest support the assumption leading to (6), the assumption is qualitative and must be remembered when considering errors in the estimated profiles in later sections. It should also be noted that the implicit limitation of having to make some assumption about the spatial dependence of number density and scatterer strength in InSAR is a limitation of virtually all remote sensing techniques: They respond to the product of the scatterer efficiency or strength and the number of scatterers per unit volume, and it is often difficult to cleanly separate the two or combine them into biologically meaningful quantities like LAD.

[14] Note from (6) that the α_z parameter is the spatial frequency of a Fourier transform of the relative vegetation density multiplied by the attenuation expression. Given that interpretation, the smallest value of $2\pi/\alpha_z$ —from the highest B/H ratio—establishes a lower limit to the size of vertical density fluctuation which can be reliably described by estimates of $Rel(z)$.

2.3. InSAR Profile Measurements: Estimates From La Selva Data

[15] Profiles are estimated from InSAR data using (6) with a specific parameterization of $Rel(z)$ as a model. The estimation proceeds by proposing a model functional form for $Rel(z)$ and identifying its parameters. For profiles estimated in Central Oregon [Treuhaft *et al.*, 2002], a Gaussian was used to model $Rel(z)$ and the Gaussian parameters of mean and standard deviation were estimated along with the InSAR phase at the ground (ϕ_0) and the peak extinction coefficient (σ_x). For the 30 tropical forest stands of La Selva, it was found that $Rel(z)$ was best modeled with 12 parameters, each of which was the constant density in

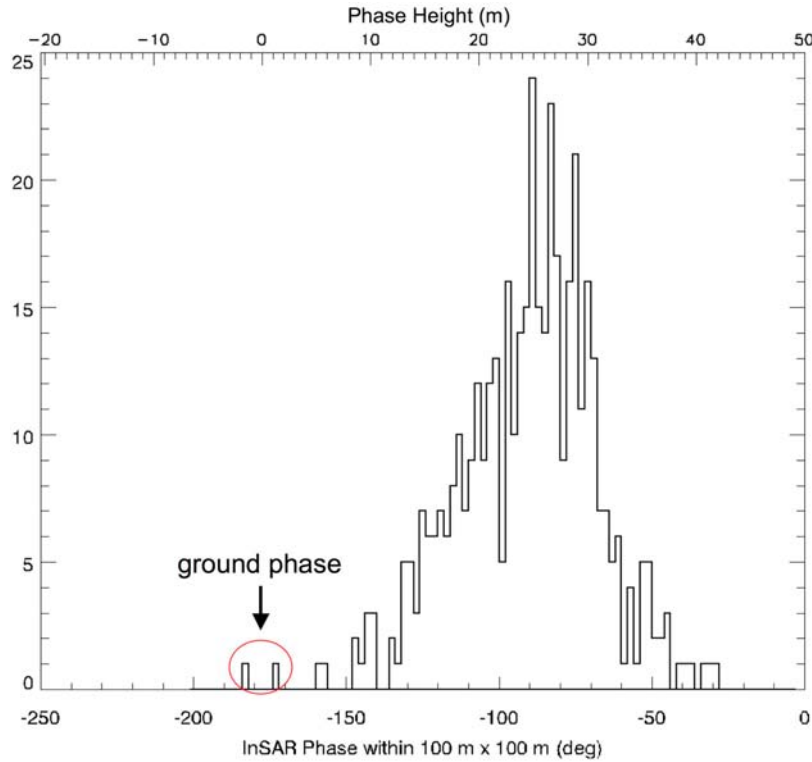


Figure 3. Histogram of interferometric phases on $5 \text{ m} \times 5 \text{ m}$ centers over a $100 \text{ m} \times 100 \text{ m}$ area surrounding a primary stand center. The red ellipse is identified as ground returns, spanning $\sim 3 \text{ m}$ in altitude, and the average of the ground returns, indicated by the arrow, is taken to be the ϕ_0 parameter. The upper axis is the phase height, which is the phase divided by α_z , which was 0.062 for this baseline. The phase height was shifted to have “0” close to “ ϕ_0 .”

5 m wide bins spanning 0 to 60 m in altitude above the forest floor (see Figure 7 for examples). With Rel_j the constant density of the j^{th} bin, the model complex coherence becomes

$$\text{Model Complex Coherence} = \frac{e^{i\phi_0} \mathcal{F}(\alpha_z)}{\mathcal{F}(0)} \text{ where}$$

$$\mathcal{F}(\alpha_z) = \sum_{j=1}^{12} \int_{(j-1)\Delta z}^{j\Delta z} dz e^{i\alpha_z z} Rel_j$$

$$\times \exp - \left[\frac{2\sigma_x}{\cos \theta} \left\{ (j\Delta z - z)Rel_j + \Delta z \sum_{k=j+1}^{12} Rel_k \right\} \right] \quad (7)$$

In (7), the bin width is Δz and is fixed to 5 m. The parameters ϕ_0 , and σ_x appear along with the set of 12 $\{Rel_j\}$ parameters in (7). Note the h_v parameter, the maximum forest height, no longer appears as it has been set to 60 m, which is 10–15 meters taller than the tallest trees observed on the ground at La Selva.

[16] Profiles were estimated by adjusting the $\{Rel_j\}$ parameters until the following expression was minimized [e.g., Hamilton, 1964]

$$\left(\vec{O} - \vec{M}(\{Rel_j\}) \right)^T \text{Cov}^{-1} \left(\vec{O} - \vec{M}(\{Rel_j\}) \right) \quad (8)$$

where \vec{O} is a vector of InSAR coherence and phase observations from 12–14 baselines, realized with multiple

aircraft altitudes described above, with corresponding α_z 's. These coherences and phases are the result of averaging complex coherences derived at $\approx 5 \text{ m}$ intervals over the $50 \text{ m} \times 50 \text{ m}$ plots. The coherences were corrected for range effects (ignored in (4) and all subsequent model expressions for complex coherence) by using vegetation-free areas outside of La Selva; they were corrected for signal-to-noise effects using the methods of *Treuhaft and Siqueira* [2000]. In (8), \vec{M} is the corresponding vector of model coherences and phases from (7) for each α_z , and Cov is the covariance matrix of the observation errors in coherence and phase, which are assumed to be independent (Cov is diagonal).

[17] While the $\{Rel_j\}$ parameters were adjusted to minimize (8), ϕ_0 and σ_x were fixed before the minimization process, based on information other than the plot-averaged complex-coherence observations. When Gaussian [*Treuhaft et al.*, 2002] or constant [*Papathanassiou and Cloude*, 2001; *Hajnsek et al.*, 2009] profiles are assumed as a model, especially with polarimetric InSAR as in the last two references, it is possible to estimate the ground phase parameter ϕ_0 from the $50 \text{ m} \times 50 \text{ m}$ plot-averaged InSAR data. But with the more complicated density parameterizations of this experiment as in (7), and in the absence of polarimetric interferometry, we found the ground return to be indistinguishable from low-altitude vegetation density, and ϕ_0 was difficult to estimate from the plot-averaged InSAR data alone. For this reason, ϕ_0 was established by examining histograms of InSAR phases on finer $\approx 5 \text{ m} \times 5 \text{ m}$ centers within a $100 \text{ m} \times 100 \text{ m}$ area around the center of

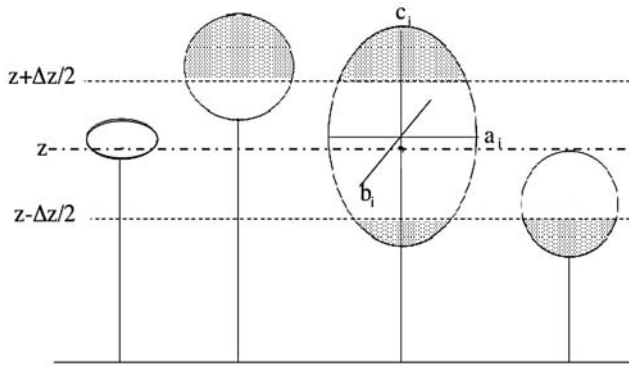


Figure 4. Field measurements of total height, height-to-base-of-crown, and lateral dimensions of the canopy (a and b) specify the volume of model ellipsoid trees contributing to field density between $z - \Delta z/2$ and $z + \Delta z/2$.

each $50 \text{ m} \times 50 \text{ m}$ plot used, as in Figure 3 for a primary stand. A collection of the lowest few phases, indicated by the red ellipse in Figure 3, was taken to be from the ground, and ϕ_0 was assigned the average value of the phases of the ground return. As α_z gets bigger (baseline length gets bigger, or aircraft altitude gets lower), the distribution of phases, which is proportional to the distribution of vegetation height, gets wider. With large enough α_z , the phases from the bottom to the top of the canopy wind through 360° , and a clear identification of the bottom as in Figure 3 is no longer discernable. The method used to “find the ground” in this paper fails, and for this reason only phases from observations with the first 5 lowest values of α_z were used in the analysis. Coherences from all α_z 's were used. Simulation demonstrates that the peak extinction parameter, σ_x , is also difficult to estimate from the InSAR data when the vegetation profile is allowed to be as multilayered as in (7) [Treuhaft *et al.*, 2009]. For this reason, 0.1 dB/m was adopted as the peak extinction for all 30 stands, because, as will be seen in sections 3 and 4, it gave the best agreement with field and lidar profiles.

[18] As suggested by Figure 2b, many different arrangements of vegetation components (many different vectors) can sum to the same total InSAR observation for a single baseline. Equivalently, a single Fourier transform of vertical structure cannot completely specify profile characteristics. Multibaseline InSAR is therefore required to isolate each component in a vegetation profile. Each baseline, with its corresponding α_z , generates a new and different Figure 2b, with the same vector lengths, but phases which scale in proportion to α_z . From multibaseline data, the individual vector lengths, which are proportional to vegetation density, can be estimated. From a parameter estimation point of view, the more detailed the profile parameterization—the more profile parameters to be estimated—the more InSAR baselines are necessary. At very least, the number of total observations (InSAR and/or others) must equal or exceed the number of independent parameters to be estimated. By flying at 7 different radar altitudes, H , up to 14 effective baselines were produced with α_z 's between 0.043 m^{-1} to 0.54 m^{-1} . Because the minimum detectable vertical scale is approximately $2\pi/\alpha_z$, we can expect vertical sensitivity on scales of 13 m and higher. That is, accurate estimation of

abrupt changes in vertical structure at scales shorter than 13 m would require larger baselines or lower altitudes than those of this experiment.

2.4. Field Profile Measurements

[19] Field measurements on the same 30 stands at La Selva along $10 \text{ m} \times 100 \text{ m}$ transects included the location of each tree in along- and cross-transect coordinates, diameter at breast height, height to the base of the crown, total height, and lateral dimensions of each tree's canopy. All tree heights were measured using ocular methods, that is, they were estimated visually. For each tree with diameter at breast height greater than 10 cm (greater than 5 cm for abandoned pastures), heights were measured by sighting along the arm to subtend angles from the bottom to the top of the tree. Vantage points were sought which optimized the visibility of the tops of trees. These visual height estimates were calibrated by clinometer measurements [Gonçalves and dos Santos, 2008]. A model was developed in Amazônia and La Selva with ocular height estimates as input and heights based on clinometer readings as output. Lateral dimensions of the canopies were estimated by stretching measuring tape between points directly beneath the extrema of the observed canopy, in the directions parallel and perpendicular to the transect. From these measurements, semimajor axes of each tree modeled as an ellipsoid were calculated as shown in Figure 4 [Nelson, 1997]. The volume of each ellipsoid overlapping an altitude bin was assumed to be uniformly filled with leaf area and summed to calculate the leaf area density at altitude z . Departures from the “uniformly filled” assumption will be addressed in section 4 on errors. For a height bin centered at z and thickness Δz , the relative field density profile was modeled as

$$\begin{aligned} \text{Field Density}(z) &\propto \sum_{i=1}^{N_z} \int_{V_i(z)} dx dy dz \\ &= \sum_{i=1}^{N_z} \int_{z_{loi}}^{z_{hii}} \pi a_i b_i \left[1 - \left(\frac{z - z_i}{c_i} \right)^2 \right] dz \quad (9) \end{aligned}$$

where $V_i(z)$ is the volume of the i^{th} tree in the height bin at z , z_i is the center of the ellipsoid representing the i^{th} tree with any part inside the bin at $z \pm \Delta z/2$, N_z is the number of trees with foliage overlapping the height bin, and a_i , b_i , and c_i are the x , y , and z semimajor axes of the ellipsoid. The integration limits z_{loi} and z_{hii} are between the lowest and highest points for the i^{th} tree within the bin.

2.5. Lidar Profile Measurements

[20] Lidar data were collected at La Selva by the Laser Vegetation Imaging Sensor [Blair *et al.*, 1999] in spring, 2005 [Blair *et al.*, 2006]. LVIS records a waveform with the complete return history of the near-infrared laser energy reflected off of different surfaces (leaves, branches, ground). At any height, the amplitude of the waveform corresponds to the relative abundance of vertically intercepted surfaces. Because of attenuation, lidar waveforms are sometimes adjusted using a modified MacArthur-Horn transformation [Harding *et al.*, 2001; Lefsky *et al.*, 2002] to produce a canopy height profile. In this study we did not transform the lidar waveforms because a previous study at this site

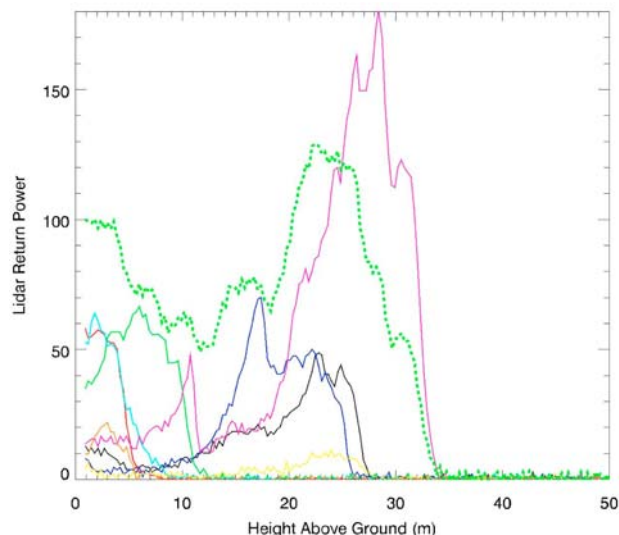


Figure 5. All lidar waveforms with beam area overlap with a secondary forest stand, 19–23 years old. Each waveform is represented by a different color and is multiplied by its fractional beam overlap with the $50 \text{ m} \times 50 \text{ m}$ stand. The dashed green line is the average of all the waveforms, multiplied by 4 for easier viewing. This average waveform was compared to InSAR and field profiles.

demonstrated that both transformed and untransformed lidar profiles (averaged within a plot) did not significantly differ from field-derived profiles and profile metrics from untransformed lidar profiles showed slightly stronger correlation with metrics from field profiles [Drake *et al.*, 2002b].

[21] Lidar profiles were produced for each of the 30 sites by averaging all waveform profiles for which any part of the

Gaussian beam fell within the $50 \text{ m} \times 50 \text{ m}$ area characterizing a site. Each waveform profile was weighted by the fractional beam overlap in the averaging process. In order to calculate the fractional overlap, each beam was considered to have Gaussian standard deviation of 6.25 m [Blair and Hofton, 1999], equivalent to a beam diameter of approximately 25 m. There were on average 11–14 shot centers within the $50 \text{ m} \times 50 \text{ m}$ areas, suggesting shot centers were separated by average linear distances of approximately 13–15 m. Each waveform was referenced to the ground level before averaging. Figure 5 shows an example of a set of waveforms and their average for a secondary stand, 19–23 years old. The lidar return power on the ordinate is the product of the actual return power and the overlap weight. It is the average waveform that is used to compare with vegetation densities derived from InSAR and field measurements. As discussed in section 4 on errors, for primary and secondary forests, this ground “bump” was difficult to find and contributed to the error in plot-averaged waveforms, especially in the overall placement of the waveform on the horizontal (altitude) axis.

3. Results

3.1. Lateral Scale of Profiles With InSAR

[22] One of the first results to emerge from the analysis of InSAR and lidar data was the specification of the lateral scale over which InSAR profiles could accurately be estimated, given our algorithmic approach to topography. The InSAR analysis algorithms written for the La Selva data first remove a planar topographic slope. The reason for this is that, like vertically extended vegetation, topographic rises within a site will cause phase to increase and coherence to decrease, relative to a flat site. The ideal lateral scale for profile estimation is one for which the removal of planar

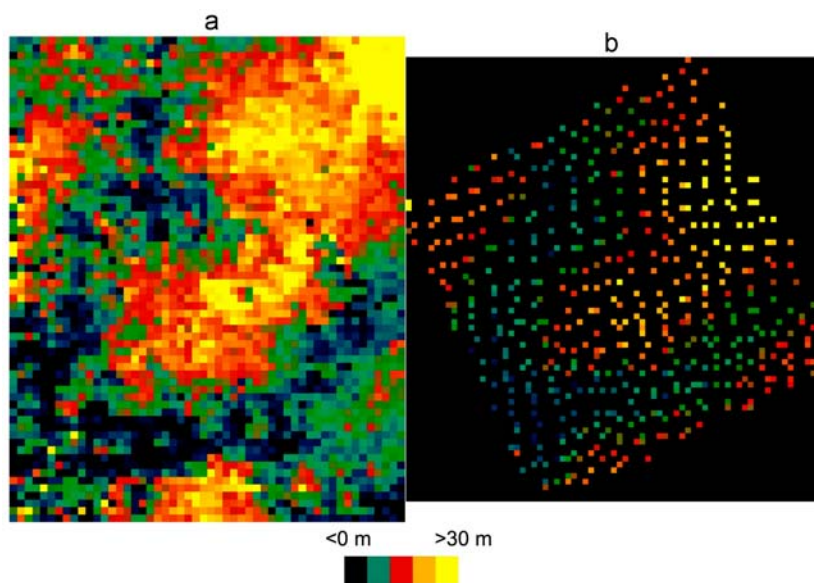


Figure 6. (a) InSAR phase height (phase divided by α_z) for a $300 \text{ m} \times 300 \text{ m}$ area surrounding one of the abandoned-pasture sites. (b) The LVIS lidar ground altitude of the same area. The lidar altitudes suggest that the higher InSAR phase at the center of the image is due to an elevation rise, not a stand of trees. Comparison of these images suggested reducing the size of the plots over which InSAR profiles would be estimated from $100 \text{ m} \times 100 \text{ m}$ to $50 \text{ m} \times 50 \text{ m}$.

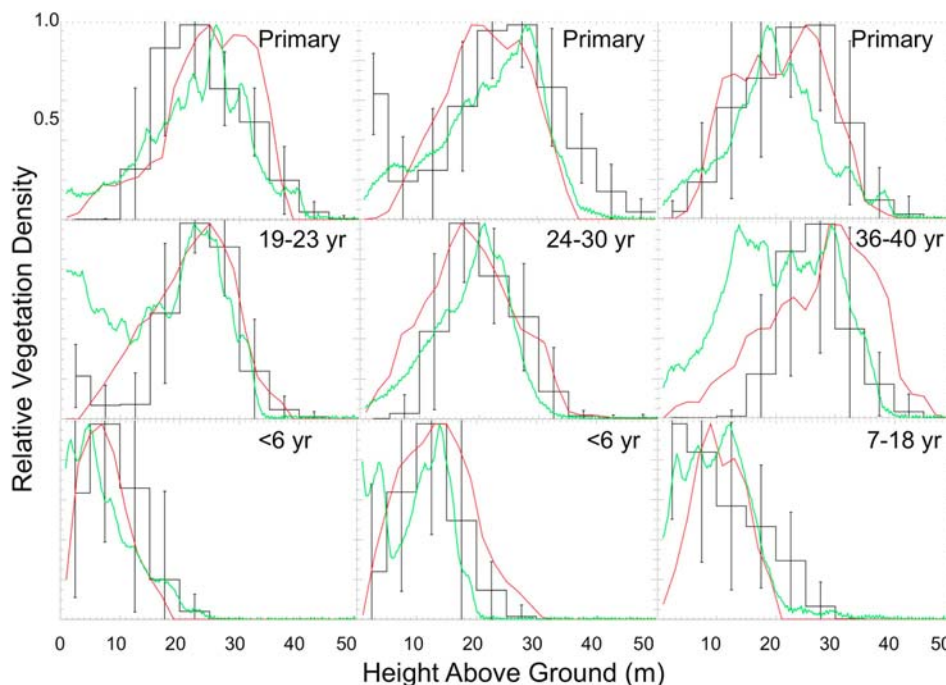


Figure 7. Relative vegetation density profiles, with each peak normalized to “1,” from multibaseline InSAR (black), field (red), and lidar (green) measurements, for nine forest stands.

topography suffices to reduce topographic effects on phase and coherence below those of vegetation structure.

[23] Figure 6 shows a $300\text{ m} \times 300\text{ m}$ area from both InSAR and lidar at La Selva. At the center of the images is one of the abandoned pasture stands with short trees and a profile-averaged vegetation height of about 10 m (the second <6 yr plot in Figure 7). The InSAR image on the left is the phase height (the phase divided by α_z), and the right-hand image shows the lidar surface topography estimate. Each lidar dot corresponds to the center of a 25 m beam of the lidar, though each dot is only $5\text{ m} \times 5\text{ m}$, like the InSAR pixels on the left. The InSAR phase height in Figure 6 shows variations of $>20\text{ m}$ within 100 m of the center of the image, suggesting either the presence of a forest with profile averaged mean vegetation heights of 20 m or rapidly varying topography. The strong correlation of the InSAR image with the lidar topography image suggests that topographic fluctuation is largely responsible for the InSAR phase height changes. Prompted by Figure 6, the original lateral scale for InSAR was reduced from $100\text{ m} \times 100\text{ m}$ to $50\text{ m} \times 50\text{ m}$. It was found that for stands such as in Figure 6, if the lateral scale exceeded $50\text{ m} \times 50\text{ m}$, the slope of the topography changed too rapidly to be removed by the planar fitting InSAR algorithms, and abandoned pastures with topography could be mistaken for secondary or primary forests. For this reason, the lateral scale adopted for all InSAR and lidar profiles was $50\text{ m} \times 50\text{ m}$. In future experiments, it may be possible to develop more complex InSAR algorithms to remove more rapidly varying topography and consider larger lateral scales. That larger lateral scales can confuse topography and tree heights is also true for large-spot lidars [Lefsky *et al.*, 2005].

3.2. Profiles and Moments From Multibaseline InSAR, Field, and Lidar Measurements

[24] Figure 7 shows estimated profiles for 9 of the $30\text{ m} \times 50\text{ m}$ stands at La Selva. The 9 stands are representative of each of the forest cover types, as indicated. The black in Figure 7 is the InSAR-estimated profile, red is the field profile, and the green is the lidar profile from the average of the waveforms, as in Figure 5. While the InSAR and lidar plots were $50\text{ m} \times 50\text{ m}$, the field profiles derived from measurements on $100\text{ m} \times 10\text{ m}$ transects. The field plot size was chosen in part because surface topography was not an error for field measurements and in part because, at the time of the field data acquisition, $100\text{ m} \times 100\text{ m}$ stands were being considered for the InSAR analysis. We observed anecdotally in the field and by doing different cuts on the lidar data that vertical structure measurements on these various lateral scales were highly correlated, but this statement should be made more quantitative in the future with auto correlation functions of structure metrics as a function of lateral distance in the forest. The InSAR profile, $\{Rel_j\}$ as in (7) is shown as stepwise constant, with 12 values of vegetation density as estimated parameters at intervals of 5 m in height. As mentioned, the extinction was fixed 0.1 dB/m, and this will be treated in the discussion of RMS agreement with field and lidar in Figure 8. Visual inspection of Figure 7 suggests that small-scale ($<10\text{ m}$ vertically) features do not agree between the three profiles; recall that InSAR accuracy for the baselines of this experiment is expected to deteriorate for fluctuations of scale less than 13 m. It also seems that a translation of one or more of the profiles on the “Height” axis would produce better agreement for some stands. The InSAR and lidar profiles incurred

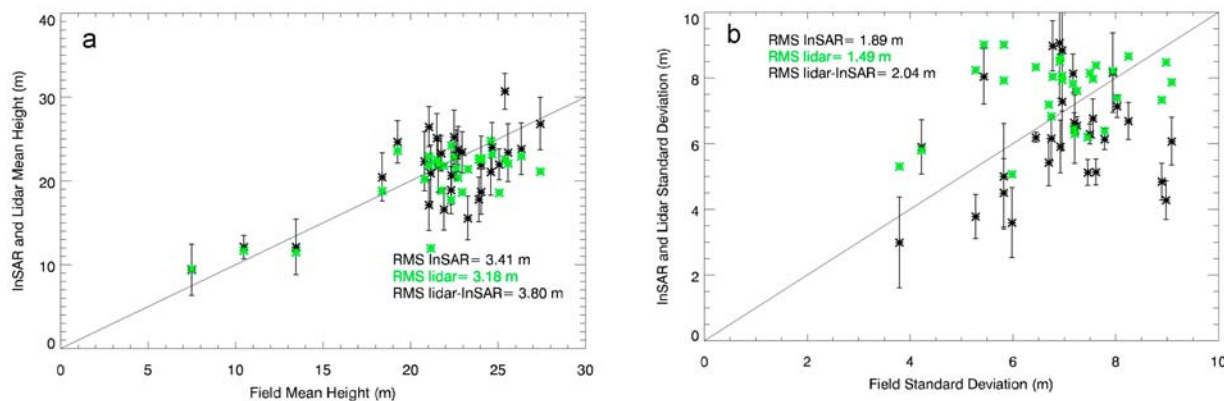


Figure 8. The (a) mean and (b) standard deviation of the vegetation distributions from InSAR (black) and lidar (green) versus field estimations, for uniformly filled ellipsoidal trees.

error due to “finding the ground”, as discussed in the next section. Larger-scale characteristics of the profiles, such as means and standard deviations appear to agree. An enhancement near zero is seen in the InSAR and lidar profiles for a number of primary and secondary profiles. All 3 abandoned pastures show vegetation density near the ground. In all cases, the enhancements near the ground are probably due to shorter trees, understory, and return from the ground itself. In order to minimize ground contamination in the analyses of Figure 8 below, the first 5 m bins of Figure 7 were reduced by 75% for the InSAR, and all powers for lidar altitudes lower than 5 m similarly reduced by 75%. Though this process seems ad hoc, various ground suppression approaches made very little difference in the quantitative analyses of Figure 8. No low-altitude enhancements are evident in the field data for primary and secondary forests primarily because field measurements do not have a “ground return”. Also, because trees with diameters less than 10 cm—5 cm for abandoned pastures—were excluded from the field study, there may be some reduction of vegetation contributions at the lowest altitudes in the field profiles. The error bars on the InSAR profiles result from dividing each stand up into 4 equal subplots and using the scatter of the InSAR observations in those subplots to first calculate the error in the InSAR observations. The distribution of InSAR observation errors is then used in a Monte Carlo process simulating a set of InSAR observations about the actual InSAR observations. From these simulated observations, estimates of standard deviations—the error bars—are derived. This approach to estimating profiles and errors ignores systematic errors common to an entire stand, which will be discussed in the next section.

[25] Figure 8 shows the mean and standard deviations of the InSAR and lidar density profiles $Rel(z)$, defined as

$$\text{Mean} = \frac{\int z Rel(z) dz}{\int Rel(z) dz}$$

$$\text{standard deviation} = \left(\frac{\int z^2 Rel(z) dz}{\int Rel(z) dz} - \text{mean}^2 \right)^{1/2} \quad (10)$$

They are plotted versus the field quantities. For lidar, $Rel(z)$ is the waveform. The RMS differences between the InSAR or lidar and field means are 3.40 m and 3.21 m, or 16% and 15% of the average mean height, respectively (see Table 1). The RMS difference between InSAR and lidar is of the same order, 3.70 m or 17%. Note the possible overestimate of field mean heights at the high end of Figure 8a, as evidenced by a preponderance of both InSAR and lidar points below the $y = x$ line. As discussed in the next section on errors, this could be due to the assumption of modeling the trees as uniformly filled ellipsoids as in (9). It could also be due to the 10 cm diameter-at-breast-height cutoff for trees included in profile estimation for tall forests. The RMS differences, if assumed equally apportioned and independent between the techniques, suggest approximately 2 m errors in mean height characterizes InSAR, field, and lidar measurements. The next section on error modeling refines that apportionment to reflect dominant modeled errors for each technique.

[26] Figure 8b shows the standard deviation of the vegetation density distribution for InSAR and lidar versus the field standard deviation. The InSAR scatter about the field measurements is 1.91 m, or 27% and the lidar scatter is 1.47 m or 21%. The scatter of the InSAR about the lidar measurement is 1.86 m or 27%.

[27] It was found that using 0.1 dB/m as σ_x in (7) for all 30 stands yielded the lowest scatters of InSAR mean and standard deviation about the field or lidar measurements in Figure 8. While there is no universally accepted value for the extinction coefficient of forest vegetation, modeled and measured values have been reported from 0.2 dB/m to

Table 1. RMS Scatters of InSAR and Lidar Profile Means and Standard Deviations About Field Values for Three Models of Field Profile Construction^a

Model	InSAR Mean (m)	Lidar Mean (m)	InSAR Standard Deviation (m)	Lidar Standard Deviation (m)
Uniform	3.4	3.2	1.9	1.5
Spoke	3.3	2.9	1.9	1.4
Spoke ²	3.9	3.3	1.9	1.3

^aModels are (1) uniformly filled volumes, (2) the “bicycle spoke” radial dependence of volume filling as in equation (12), and (3) the spoke² model, where the filling is inversely proportional to the radial distance squared (equation (12) with the denominator squared).

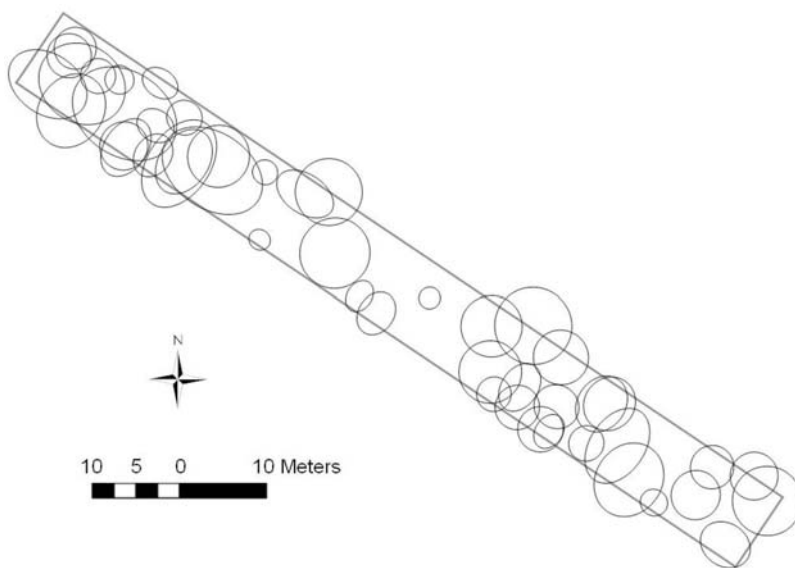


Figure 9. The distribution of crowns from field measurements along a 10×100 m transect in a primary forest. The ellipse for each crown has semimajor and semiminor axes as measured in the field. Trees tend to be clumped, with substantial lateral gaps of bare terrain.

beyond 1.0 dB/m [Chuah and King, 1994; Papathanassiou and Cloude, 2001; Bosisio and Dechambre, 2004]. Our extinction coefficient of 0.1 dB/m could be low because it represents an average over $50 \text{ m} \times 50 \text{ m}$ of forest structure, which, even in primary forests, contains substantial lateral gaps with very little vegetation. Figure 9 shows an example of field-measured canopy dimensions (ellipses with a_i and b_i of Figure 4), with centers placed as measured along one of the field transects of a primary stand at La Selva. Trees are not uniformly spread on the transect, but rather there are clear regions near the center of Figure 9 in which the radar beam would detect returns near the ground. The ground returns and returns from the trees in the clumps would contribute vectors with small phases and very large phases, respectively, in Figure 2. A large diversity of altitudes for the returns would lower coherence, which, in turn, could make the vertical extent of returns seem large, signaling high penetration or low effective extinction. In other words, these clear regions of zero vegetation density may create an average density, and therefore average attenuations via (4), lower than that characteristic of the forest vegetation in the clumps of trees in Figure 9. The observational signature of a taller canopy is a lower coherence and a higher phase. If the coherence dropped due to instrumental effects, but the phase remained the same, the estimated extinction coefficient might decrease, also in part explaining our low value of 0.1 dB/m.

[28] As mentioned in subsection 2.1, 6 of the primary forest stands were selectively logged, according to La Selva records. However, field measurements failed to detect logging “scars”—tree stumps, skid trails, or felling gaps—in these areas. We plan to resolve this apparent discrepancy with La Selva records in a future publication. Preliminarily, foliage height diversities derived from InSAR as in (1) from those 6 stands were approximately 10% lower than those of the other primary stands. A detailed analysis

of FHD and biomass estimates will appear in a future publication on products derived from profiles.

4. Dominant Errors in the InSAR, Field, and Lidar Measurements

[29] This section explores some of the dominant errors in the InSAR, field, and lidar measurements in order to understand the empirical profile-averaged mean height scatters of the last section. The dominant errors considered suggest InSAR and field mean-height errors of 3 m, while the lidar mean-height errors are 2 m. At the 25% level, these dominant modeled errors overestimate the 3.4 m RMS scatter in the differenced means in Figure 8a, which suggests that the modeled errors account for the observed scatters, but are perhaps too conservative. While a complete error analysis of each of the three techniques is beyond the scope of this paper, this section shows that the scatters between the techniques are plausibly attributed to known dominant error sources.

4.1. InSAR Errors

[30] Phase and coherence calibration errors lead to errors in profiles estimated from InSAR. An origin of phase, ϕ_0 , as in Figure 3 must be determined for each baseline. Due to the relatively flat terrain in Oregon, that analysis used nearby clear areas to arrive at the ground surface phase [Treuhaft *et al.*, 2002]. At La Selva, the nearest clear areas were outside of the white line on Figure 1. Because there were frequently substantial topographic changes between the clear areas and the forest stands, and because there seemed to be instrumental phase drifts—probably due to uncompensated aircraft motion—over the substantial distances between clear and forested areas, using the clear areas to establish ϕ_0 did not perform well. As mentioned, the process illustrated in Figure 3, using the set of InSAR phases *within* an extended, $100 \text{ m} \times 100 \text{ m}$ stand to equate the lowest to ϕ_0 gave more

consistent results. However, this process adds a level of subjectivity and human error, which is probably at the 5 meter level per baseline, of the order of the dimensions of the red ellipse indicating the ground return. The conversion of phase to meters of altitude for the baseline of Figure 3 ($\alpha_z = 0.062$) is shown on the top x axis. An error in ϕ_0 , if it is proportional to α_z for each baseline, would move the entire profile up or down on the x axis. But since the “finding the ground” phase calibration error is probably independent between baselines, the final average-height error can be estimated by dividing the 5 m per baseline error by the square root of the number of baselines in which phase was used (5), yielding 2.7 m. Note that this is an approximate estimate, as the actual error depends on the parameter estimation process in the minimization of (8).

[31] The coherence as well required calibration for each baseline, which involves accounting for loss of coherence due to noise and so-called “range decorrelation” [Rodriguez and Martin, 1992; Treuhaft et al., 1996], as well as any other instrumental errors in the processing of signals at each end of the baseline. The clear, farm areas outside of La Selva were used in the coherence calibration process. For the range of α_z 's in this experiment, 0.043 m^{-1} to 0.54 m^{-1} , an estimate of the coherence calibration error is based on the difference between coherences of the 2–3 clear areas used to calibrate each baseline, which was of the order of 2% to 10% from the lowest to highest α_z 's. In order to get an approximate estimate of the effect on mean-height estimates due to this level of coherence error, consider the coherence from a simplified, uniform vegetation layer without attenuation. For a forest height h_v , the coherence for the zero-extinction uniform layer is (from (4) with the imaginary part of the forward scattering amplitude set to zero, and the number density and backscattering vertical dependence taken to be uniform; or from Treuhaft et al. [1996])

$$\text{Coherence} = \frac{\sin \alpha_z \frac{h_v}{2}}{\alpha_z \frac{h_v}{2}} \quad (11)$$

By taking derivatives of (11) with respect to $h_v/2$, it can be demonstrated that a 1 m change in average tree height for a 35 m stand corresponds to a change in coherence of about 1% to 5% over the range of baselines in this experiment, from the lowest to the highest α_z 's. Thus each of the 12–14 coherences used contributes about 2 m error. The net error again can be estimated by dividing this error by the square root of the number of baselines, yielding 0.6 m. This estimate is approximate for the same reasons mentioned above for the phase calibration error estimate, and additionally because it uses the uniform-volume expression in (11), which, according to Figure 7, does not accurately describe the stands at La Selva.

[32] Considering this assessment of the phase and coherence error contributions, an overall approximate calibration error of 3 m seems reasonable for mean heights. Note that the average error bar in Figure 8a, which is empirically determined, is 2.8 m, suggesting that the phase and coherence errors considered account for much of the observed error.

[33] One other source of error already mentioned, but not modeled in the above considerations, is the assumption that

the average backscattering intensity per scatterer, $\langle f_b^2(z) \rangle$, in (5) is independent of z , which leads to (6). If the backscattering intensity does have vertical dependence, it will cause errors in the estimates of $Rel(z)$. Though beyond the scope of this paper, a complete analysis of this possibility could involve proposing plausible functional dependences of $\langle f_b^2(z) \rangle$, generating simulated data using (5), and analyzing the data using the parameterization of (7). The level of agreement between InSAR and field measurements discussed in Table 1 suggests that the error due to assuming the uniformity of $\langle f_b^2(z) \rangle$ is probably not as big as the phase and coherence errors considered above. Another approach to profile estimation has been to combine all the terms to the right of $\exp(i\alpha_z z)$ in (4) into a single profile of the strength of the returned radar signal [e.g., Cloude, 2007]. While estimating this profile does not uniquely separate vegetation density from scatterer brightness and attenuation, as in (2), it may be that for many applications, the radar signal profiles have useful correlation with biological properties of the forest, such as biomass.

4.2. Field Errors

[34] As mentioned in section 2.4, ocular methods for measuring tree heights in the field, which were then used in integration limits in (9), were calibrated with a clinometer. The ocular measurements were determined to be accurate to 1 m in the vertical direction and 0.5 m in the lateral directions [Gonçalves and dos Santos, 2008]. Another source of error in profiles estimated from field measurements is the form of (9) itself, which assumes that leaf area uniformly fills the ellipsoids described by the dimensions measured in the field. We tested a second model that assumed a decrease in leaf area as a function of the radial distance from the trunks, similar to the linear density of bicycle spokes, which decreases with radial distance from the axle. Physically, the “spoke” model assumes that the density of leaves surrounding each branch is approximately uniform, and that the gaps between the branches of uniform vegetation are formed by the radial spread of the branches, or spokes, themselves, resulting in an average 1/radius dependence of density. The spoke model can be written as

$$\text{Field Density}(z) \propto \sum_{i=1}^{N_z} \int_{V_i(z)} \frac{dx dy dz}{\sqrt{(x^2 + y^2)}} \quad (12)$$

where $V_i(z)$ is as in (9). Because taller trees tend to have canopies with larger lateral extents, the uniform-filling model increases the leaf area density at higher altitudes relative to the spoke model. We also tried a spoke² model, with the denominator of (12) squared. The spoke² model assumes that leaves decrease in volume occupied per branch as the distance from the trunk increases. There is no a priori physical reason to assume the spoke² model; it is merely shown to span a number of possibilities for radial dependence. Ultimately it would be better to base the 3-D (not just radial) volume filling characteristics of leaf area on field data of the type indicated by Bongers, 2001. In the examples shown in that reference [Sinoquet and Rivet, 1997], it is clear that leaf area density, for the specific species chosen, exhibits a radial dependence, but it is not strictly linear, as in the spoke model. Perhaps future work

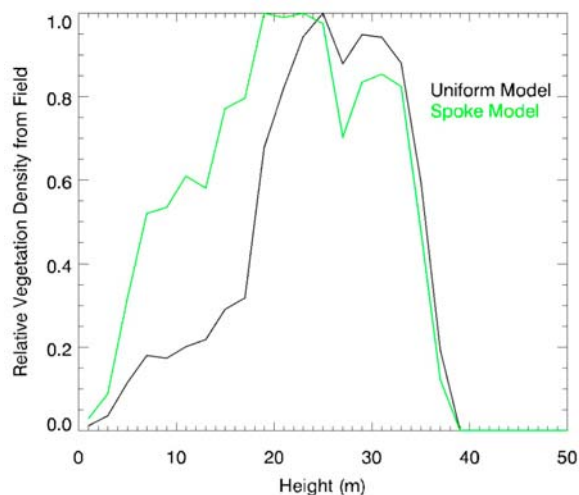


Figure 10. The relative field-estimated density for a primary stand using the uniformly filled volume model (black) and the spoke model (green). The mean of the black curve is 24.6 m, and that of the green curve is 21.2 m.

might entail complete studies characterizing the volume filling characteristics, of the sort indicated by Bongers [2001], but extended to the multiple species of a tropical forest.

[35] Table 1 shows the RMS scatters of the InSAR and lidar means and standard deviations about the corresponding field-measured quantities for the uniform-filling model (9), the bicycle spoke model (12), and the spoke² model. The spoke model gives smaller RMS scatters from InSAR (3.3 m) and lidar (2.9 m), but the spoke² model is about the same or worse than the uniform model for most of the entries of Table 1. From Table 1, it seems that the optimal model includes a radial dependence of leaf area which is somewhere between the uniform-volume and spoke² model, and closer to the spoke model. An example of the difference in the ground profiles using the uniform or spoke model is

shown in Figure 10. The mean changes from 24.6 m for the uniform model to 21.2 for the spoke model. In general, shifts of 3 meters seem reasonable as an error accounting for both height measurement error and possible volume-filling mismodeling.

4.3. Lidar Errors

[36] As in Figure 5, all the lidar waveforms within $50\text{ m} \times 50\text{ m}$ areas must be averaged to produce the average profile. For each waveform, the ground must be identified and the waveform positioned on the x axis to be “zero” at the ground. The difficulty in finding the ground for some of the waveforms induced a significant error in the lidar profiles. LVIS data taken in 1998 over La Selva [Blair *et al.*, 2004] were compared to LVIS data taken in 2005 in order to characterize the different presentations of the ground signal. For the same primary stand, Figures 11a and 11b show the waveforms that were averaged together to produce the profile, offset by about 7 meters from the expected ground location, for the 1998 and 2005 data respectively. Note that the 2005 data were used in Figure 7 and throughout this paper because they were closest in epoch to the InSAR and field measurements and because all of the stands of Figure 1 had analyzed lidar shots, while only about half of our stands showed lidar shots in the 1998 data. For both data sets, a ground-finding algorithm searched for a maximum within a 10 m range specified near the point where obvious ground peaks were detected. The point of the expected ground enhancement, $\pm 2\text{ m}$, is shown on the x axis with arrows. Enhancements are obvious for almost all of the 1998 waveforms in Figure 11a in the neighborhood of the arrows. In Figure 11b for the 2005 data, however, it is difficult to see ground enhancements for any of the waveforms. For all stands, the algorithm was constrained to find a ground bump up to a maximum altitude on the x axis. When there was no obvious bump, as in Figure 11b, the upper limit was set to a single value, established by examining the onset of the signal for all such stands. By varying that upper limit over plausible ranges of uncertainty, it was determined that the difficulty in finding

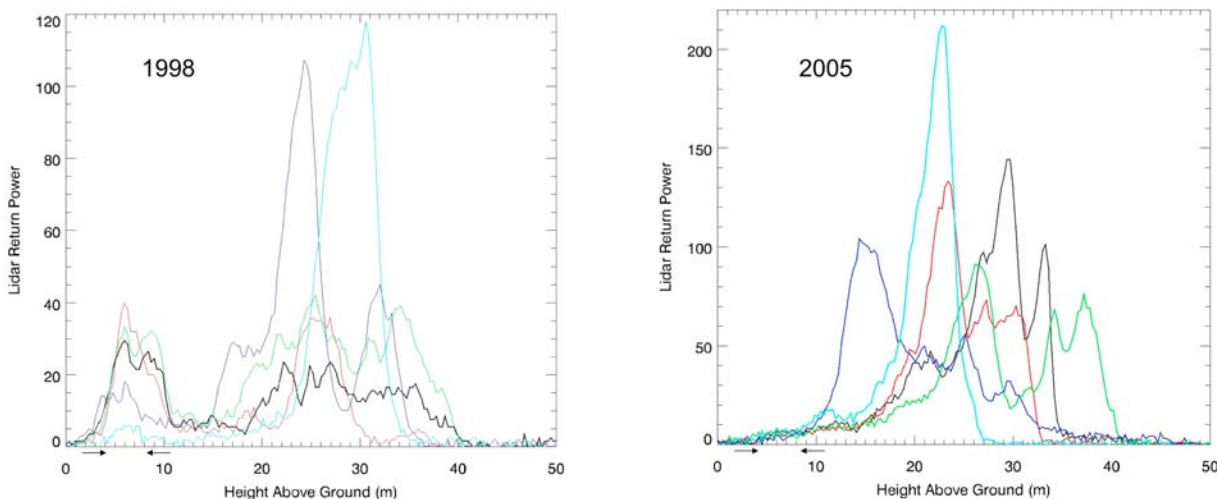


Figure 11. For a primary stand, lidar return power (not weighted by area overlap) versus height for the same stand in 1998 and 2005. Unlike Figure 5, only shots with centers within the $50\text{ m} \times 50\text{ m}$ stand are shown. Each color represents a different shot. The arrows show the expected ground altitude $\pm 2\text{ m}$.

the origin for lidar waveforms induced a 2 meter error in lidar mean heights. Reasons why ground returns may have been more difficult to detect in 2005 include 1) the increase in swath width from 1 to 2 km in the LVIS data acquisition of 2005, requiring larger incidence angles, 2) drier conditions in 1998 than 2005, resulting in more leaf loss and possibly greater penetration in 1998, and 3) growth of canopy and understory presenting more leaf area in 2005.

5. Conclusions

[37] InSAR complex coherence measurements with 12–14 baselines at C band over 30 tropical forest stands at La Selva have yielded vegetation profiles in agreement with field and lidar profiles for large-scale vertical features. Based on simple modeling considerations, these profiles are interpreted as leaf area density profiles at C band. Agreement between InSAR and lidar was at the 3.4 m level for mean and 1.9 m level for standard deviation, as shown in Table 1. The low extinction coefficient of 0.1 dB/m, which yielded the best InSAR agreement field and lidar measurements, may in part be due to the presence of lateral clumps of trees, exposing bare soil or undergrowth. As in Figure 9, the correlated rather than homogenous nature of the lateral distribution of trees may have induced an effective extinction coefficient over the 50 m × 50 m plots much lower than that through the densest foliage in tropical forests.

[38] Principal errors of phase and coherence calibration for InSAR were modeled to be at the 3 m level, with the dominant error being phase—“ground finding”—calibration errors. The principal coherence error had to do with accounting for coherence losses which tend to make stands seem more vertically distributed and/or less absorptive. Dominant field errors included ocular measurement error, but were principally due to the assumption of the uniformly filled volume. The net field error was estimated to be 3 m for the average height. A principal error for the lidar data was also related to finding the ground, inducing 2 m profile-averaged height errors. The above modeled errors are equivalent to 14% mean-height errors for InSAR and field, and 9% for lidar. These errors account reasonably well—within 25%—for the observed scatters in Figure 8a between InSAR and field mean heights (16%), lidar and field (15%), InSAR and lidar (18%), but generally overestimate the scatters observed.

[39] For the profile standard deviations, the scatters in Figure 8b were 27% and 21% for InSAR and lidar about field measurements. Though a detailed error analysis for standard deviations was not performed, if one assumes that the InSAR, field, and lidar errors were in the same 3:3:2 ratio as for the mean heights and uses the 1.89 m scatter for the InSAR-field standard deviations of Figure 8b as a normalization, the InSAR and field profile standard deviation errors are 1.3 m (19%), and the lidar error is 0.9 m (13%), which reproduces the observed scatters of Figure 8b within 10%. Note that the InSAR and lidar error quotes, and the inferred biomass estimation accuracies below, apply to the specifics of this experiment, and, with optimized recon-figurations, might be reduced in other experimental or operational scenarios.

[40] For biomass estimation approaches linearly dependent on structural attributes [e.g., Drake et al., 2002a;

Treuhaft et al., 2003; Neeff et al., 2005], these results suggest a contribution of approximately 14–19% to biomass estimation accuracy from InSAR remote sensing alone, and 9–13% from lidar, not considering allometric conversions between remotely sensed structure and biomass. For high biomass stands, particularly in the tropics, even if allometric errors contributed another 20% error per hectare, the resulting 30% biomass estimation accuracy per hectare for the InSAR in this experiment would be close to the state-of-the-art and constitute a significant contribution to global biomass monitoring. Lidar errors plus allometric errors at this level would result in a net 24% error if lidar were used for global sampling. However, these error estimates do not take into account the likely scenario that some form of structure and power measurement will yield the optimal biomass estimate, as mentioned in section 1.1. For fire-spread rates, regional and local climate assessment, and biodiversity monitoring, the required forest-structure remote sensing accuracies seem uncertain at this point.

[41] InSAR phase calibration errors can potentially be reduced by using polarimetric InSAR at L band. Both the increased vegetation penetration at L band and the enhanced ability of polarimetric InSAR to detect the ground surface [Papathanassiou and Cloude, 2001; Garestier et al., 2006] will potentially mitigate the phase calibration error due to problems in establishing the ground level encountered in this work. L band repeat-track polarimetric InSAR data have been acquired at La Selva for the same sites as in this paper, and they will be analyzed to test the increased performance in profile estimation. Improvements to the analysis algorithms could include accounting for the vertical and lateral correlations of vegetation density. The current analysis only used vegetation volume models in which the locations and characteristics of vegetation elements were uncorrelated [Treuhaft et al., 1996]. The biological nature of the profiles measured at L band, whether or not they can still be interpreted as leaf area density, will also be considered. It is possible that smaller numbers of baselines can be used to measure moments (mean, standard deviation, skewness) or other functions of profiles [e.g., Cloude, 2007]. The possibility of economizing on the number of baselines for the purposes of space-based mission design will be considered with the L band repeat-track data. Multiple-frequency InSAR observations, such as the P and X band work of Neeff et al. [2005], can potentially reduce the number of baselines required to produce information on vertical profiles. For the field measurements, upward looking lidars may improve the accuracy of height and lateral dimension measurements [Strahler et al., 2008]. Verifying the “spoke” model for volume filling, or measuring the radial dependence of leaf area density, could potentially improve the performance of the field profile estimates. More sophisticated canopy models [Cescatti, 1997] may provide field profiles which will better calibrate the InSAR and lidar in the future. Both multiwavelength lidar and better modeling of the lidar signal return might improve the lidar profile accuracy. Restricting lidar acquisitions to near-nadir incidence angles will, in all likelihood, improve the lidar performance.

[42] The experiment described here should be repeated on other types of tropical forests. For example, the performance of the methods of this paper for the higher biomass stands of

the moist tropical forests of Amazonia could be different from that observed for the wet tropical forest of La Selva.

[43] **Acknowledgments.** The research described in this paper was carried out in part at the Jet Propulsion Laboratory, California Institute of Technology, under a contract with the National Aeronautics and Space Administration. We gratefully acknowledge the support of the Terrestrial Ecology Program, managed by Diane Wickland for the National Aeronautics and Space Administration's Science Mission Directorate. We also acknowledge cooperation with the Brazilian Research Council under grant 308253/2008-6. We thank Danilo Vargas Ramírez and Walter Cruz Cambroneiro of La Selva Biological Station for invaluable assistance with field measurements. Thanks also go to Marcia Snyder and the La Selva Biological Station GIS laboratory for assistance with the coordination of the InSAR and field measurements, and for providing the QuickBird image in Figure 1. We thank David Clark of La Selva for suggesting flight lines for the AirSAR acquisition. We also thank Ralph Dubaya for suggestions on analysis strategies for the lidar data and J. Bryan Blair for the delivery and explanation of the 2005 LVIS data. We are grateful to Lawrence Young of Jet Propulsion Laboratory for a careful reading of the manuscript and numerous helpful suggestions.

References

- Asner, G. P. (2001), Cloud cover in Landsat observations of the Brazilian Amazon, *Int. J. Remote Sens.*, 22(18), 3855.
- Asrar, G., R. B. Myneni, and E. T. Kanemasu (1989), Estimation of plant-canopy attributes from spectral reflectance measurements, in *Theory and Applications of Optical Remote Sensing*, edited by G. Asrar, p. 264, John Wiley, Hoboken, N. J.
- Blair, J. B., and M. A. Hofton (1999), Modelling laser altimeter return waveforms over complex vegetation using high-resolution elevation data, *Geophys. Res. Lett.*, 26(16), 2509.
- Blair, J. B., D. L. Rabine, and M. A. Hofton (1999), The Laser Vegetation Imaging Sensor (LVIS): A medium-altitude, digitization-only, airborne laser altimeter for mapping vegetation and topography, *ISPRS J. Photogram. Remote Sens.*, 54, 115.
- Blair, J. B., M. A. Hofton, and D. L. Rabine (2004), Processing of NASA LVIS elevation and canopy (LGE, LCE and LGW) data products, version 1.0, report, NASA Goddard Space Flight Cent., Greenbelt, Md. (Available at <http://lvis.gsfc.nasa.gov>)
- Blair, J. B., M. A. Hofton, and D. L. Rabine (2006), Processing of NASA LVIS elevation and canopy (LGE, LCE and LGW) data products, version 1.01, report, NASA Goddard Space Flight Cent., Greenbelt, Md. (Available at <http://lvis.gsfc.nasa.gov>)
- Bongers, F. (2001), Methods to assess tropical rain forest canopy structure: An overview, *Plant Ecol.*, 153, 263.
- Bosisio, A. V., and M. Dechambre (2004), Predictions of microwave attenuation through vegetation: A comparison with measurements, *Int. J. Remote Sens.*, 25(19), 3973.
- Bradbury, R. B., R. A. Hill, D. C. Mason, S. A. Hinsley, J. D. Wilson, H. Baltzer, G. Q. A. Anderson, M. J. Whittingham, I. J. Davenport, and P. E. Bellamy (2005), Modeling relationships between birds and vegetation structure using airborne LiDAR data: A review with case studies from agricultural and woodland environments, *Ibis*, 147, 443.
- Camargo, J. L. C., and V. Kapos (1995), Complex edge effects on soil moisture and microclimate in central Amazonian forest, *J. Trop. Ecol.*, 11, 205.
- Cescatti, A. (1997), Modeling the radiative transfer in discontinuous canopies of asymmetric crowns. I. Model structure and algorithms, *Ecol. Modell.*, 101, 263.
- Chen, J., S. C. Saunders, T. R. Crow, R. J. Naiman, K. D. Brosofske, G. D. Mroz, B. L. Brookshire, and J. F. Franklin (1999), Microclimate in forest ecosystem and landscape ecology, *BioScience*, 49(4), 288.
- Chuah, H. T., and W. L. King (1994), A microwave propagation model for estimation of effective attenuation coefficients in a vegetation canopy, *Remote Sens. Environ.*, 50, 212.
- Cloude, S. R. (2007), Dual-baseline coherence tomography, *IEEE Geosci. Remote Sens. Lett.*, 4(1), 127.
- Cloude, S. R., and K. P. Papathanassiou (1998), Polarimetric SAR interferometry, *IEEE Trans. Geosci. Remote Sens.*, 36(5), 1551.
- Cochrane, M. A. (2003), Fire science for rain forests, *Nature*, 421, 913.
- Cochrane, M. A., and M. D. Schulze (2003), Fire as a recurrent event in tropical forests of the eastern Amazon: Effects on forest structure, biomass, and species composition, *Biotropica*, 31(1), 2.
- Dobson, M. C., F. T. Ulaby, T. LeToan, A. Beaudoin, E. S. Kasischke, and N. Christensen (1992), Dependence of radar backscatter on coniferous forest biomass, *IEEE Trans. Geosci. Remote Sens.*, 30(2), 412.
- dos Santos, J. R., C. C. Freitas, L. S. Araujo, L. V. Dutra, J. C. Mura, F. F. Gama, L. S. Soler, and S. J. S. Sant'Anna (2003), Airborne P-band SAR applied to the aboveground biomass studies in the Brazilian tropical rain forest, *Remote Sens. Environ.*, 87, 482.
- Drake, J. B., R. O. Dubayah, D. B. Clark, R. G. Knox, J. B. Blair, M. A. Hofton, R. L. Chazdone, J. F. Weishampel, and S. D. Prince (2002a), Estimation of tropical forest structural characteristics using large-footprint lidar, *Remote Sens. Environ.*, 79, 305.
- Drake, J. B., R. O. Dubayah, R. G. Knox, D. B. Clark, and J. B. Blair (2002b), Sensitivity of large-footprint lidar to canopy structure and biomass in a neotropical rain forest, *Remote Sens. Environ.*, 81, 378.
- Garestier, F., P. Dubois-Fernandez, X. Dupuis, and I. Hajnsek (2006), PolInSAR analysis of X-band data over vegetated and urban areas, *IEEE Trans. Geosci. Remote Sens.*, 44(2), 356.
- Gonçalves, F. G., and J. R. dos Santos (2008), Composição Florística e estrutura de uma unidade de manejo florestal sustentável na Floresta Nacional do Tapajós, Para, *Acta Amazonica*, 38(2), 229.
- Hajnsek, I., F. Kugler, S.-K. Lee, and K. P. Papathanassiou (2009), Tropical forest parameter estimation by means of Pol-InSAR: The INDREX-II campaign, *IEEE Trans. Geosci. Remote Sens.*, 47(2), 481.
- Hamilton, W. C. (1964), *Statistics in Physical Science*, Ronald Press, New York.
- Harding, D. J., M. A. Lefsky, G. G. Parker, and J. B. Blair (2001), Laser altimeter canopy height profiles methods and validation for closed-canopy, broadleaf, forests, *Remote Sens. Environ.*, 76, 283.
- Holdridge, L. R. (1947), Determination of world plant formations from simple climatic data, *Science*, 105, 367.
- Houghton, R. A. (2005), Aboveground forest biomass and the global carbon balance, *Global Change Biol.*, 11, 945.
- Imhoff, M. L. (1995), Radar backscatter and biomass saturation: Ramifications for global biomass inventory, *IEEE Trans. Geosci. Remote Sens.*, 33(2), 511.
- Imhoff, M. L., T. D. Sisk, A. Milne, G. Morgan, and T. Orr (1997), Remotely sensed indicators of habitat heterogeneity: Use of synthetic aperture radar in mapping vegetation structure and bird habitat, *Remote Sens. Environ.*, 60, 217.
- Ishimaru, A. (1978), *Propagation and Scattering in Random Media*, vol. 1, Academic Press, San Diego, Calif.
- Lefsky, M. A., W. B. Cohen, G. G. Parker, and D. J. Harding (2002), Lidar remote sensing for ecosystem studies, *BioScience*, 52(1), 19.
- Lefsky, M. A., D. J. Harding, M. Keller, W. B. Cohen, C. C. Carabajal, F. D. B. Espírito-Santo, M. O. Hunter, and R. de Oliveira Jr. (2005), Estimates of forest canopy height and aboveground biomass using ICESat, *Geophys. Res. Lett.*, 32, L22S02, doi:10.1029/2005GL023971.
- Le Toan, T., S. Quegan, I. Woodward, M. Lomas, N. Delbart, and G. Picard (2004), Relating radar remote sensing of biomass to modeling of forest carbon budgets, *Clim. Change*, 67, 379.
- Lucas, R. M., N. Cronin, A. Lee, M. Moghaddam, C. Witte, and P. Tickle (2006), Empirical relationships between AIRSAR backscatter and LiDAR-derived forest biomass, Queensland, Australia, *Remote Sens. Environ.*, 100, 407.
- Luckman, A., J. Baker, M. Honzák, and R. Lucas (1998), Tropical forest biomass density estimation using JERS-1 SAR: Seasonal variation, confidence limits, and application to image mosaics, *Remote Sens. Environ.*, 63, 126.
- MacArthur, R. H., and J. W. MacArthur (1961), On bird species diversity, *Ecology*, 42(3), 594.
- McDade, L. A., K. S. Bawa, H. A. Hespenheide, and G. S. Hartshorn (Eds.) (1994), *La Selva: Ecology and Natural History of a Neotropical Rain Forest*, Univ. of Chicago Press, Chicago, Ill.
- Moghaddam, M., S. Durden, and H. Zebker (1994), Radar measurement of forested areas during OTTER, *Remote Sens. Environ.*, 47, 154.
- Mutlu, M., S. C. Popescu, C. Stripling, and T. Spenceer (2008), Mapping surface fuel models using lidar and multispectral data fusion for fire behavior, *Remote Sens. Environ.*, 112, 274.
- Neeff, T., L. V. Dutra, J. R. dos Santos, C. C. Freitas, and L. S. Araujo (2005), Tropical forest measurement by interferometric height modeling and P-band radar backscatter, *For. Sci.*, 51(6), 585.
- Nelson, R. (1997), Modeling forest canopy heights: The effects of canopy shape, *Remote Sens. Environ.*, 60, 327.
- Papathanassiou, K. P., and S. R. Cloude (2001), Single-baseline polarimetric SAR interferometry, *IEEE Trans. Geosci. Remote Sens.*, 39(11), 2532.
- Ray, D., D. Nepstad, and P. Moutinho (2005), Micrometeorological and canopy controls of fire susceptibility in a forested Amazon landscape, *Ecol. Appl.*, 15, 1664.
- Reigber, A., and A. Moreira (2000), First demonstration of airborne SAR tomography using multibaseline L-band data, *IEEE Trans. Geosci. Remote Sens.*, 38(5), 2142.

- Rodriguez, E., and J. M. Martin (1992), Theory and design of interferometric synthetic aperture radars, *IEE Proc., Part F*, 139(2), 147.
- Saatchi, S., K. Halligen, D. G. Despain, and R. L. Crabtree (2007), Estimation of forest fuel load from radar remote sensing, *IEEE Trans. Geosci. Remote Sens.*, 46(6), 1726.
- Sarabandi, K., and Y. C. Lin (2000), Simulation of interferometric SAR characterizing the scattering phase center of forest canopies, *IEEE Trans. Geosci. Remote Sens.*, 38, 115.
- Saugier, B., J. Roy, and H. A. Mooney (2001), Estimations of global terrestrial productivity: Converging toward a single number?, in *Terrestrial Global Productivity*, edited by J. Roy, B. Saugier, and H. A. Mooney, p. 543, Academic Press, San Diego, Calif.
- Schlesinger, W. H. (1991), *Biogeochemistry: An Analysis of Global Change*, Academic Press, San Diego, Calif.
- Shukla, J., C. Nobre, and P. Sellers (1990), Amazon deforestation and climate change, *Science*, 247, 1322.
- Sinoquet, H., and P. Rivet (1997), Measurement and visualization of the architecture of an adult tree based on a three-dimensional digitizing device, *Trees*, 11, 265.
- Skowronski, N., K. Clark, R. Nelson, J. Hom, and M. Patterson (2007), Remotely sensed measurements of forest structure and fuel loads in the pinelands of New Jersey, *Remote Sens. Environ.*, 108, 123.
- Slatton, K. C., M. M. Crawford, and B. L. Evans (2001), Fusing interferometric radar and laser altimeter data to estimate surface topography and vegetation heights, *IEEE Trans. Geosci. Remote Sens.*, 39(11), 2470.
- Steininger, M. K. (2000), Satellite estimation of tropical secondary forest aboveground biomass: Data from Brazil and Bolivia, *Int. J. Remote Sens.*, 21(6), 1139.
- Strahler, A. H., et al. (2008), Retrieval of forest structural parameters using a ground-based lidar instrument (Echidna[®]), *Can. J. Remote Sens.*, 34, Suppl. 2, S426.
- Thompson, A. R., J. M. Moran, and G. W. Swenson (1986), *Interferometry and Synthesis in Radio Astronomy*, John Wiley, Hoboken, N. J.
- Treuhaft, R. N., and P. R. Siqueira (2000), Vertical structure of vegetated land surfaces from interferometric and polarimetric radar, *Radio Sci.*, 35(1), 141.
- Treuhaft, R. N., S. N. Madsen, M. Moghaddam, and J. J. Van Zyl (1996), Vegetation characteristics and surface topography from interferometric radar, *Radio Sci.*, 31, 1449.
- Treuhaft, R. N., G. P. Asner, and B. E. Law (2002), Forest leaf area density profiles from the quantitative fusion of radar and hyperspectral data, *J. Geophys. Res.*, 107(D21), 4568, doi:10.1029/2001JD000646.
- Treuhaft, R. N., G. P. Asner, and B. E. Law (2003), Structure-based forest biomass from fusion of radar and hyperspectral observations, *Geophys. Res. Lett.*, 30(9), 1472, doi:10.1029/2002GL016857.
- Treuhaft, R. N., B. E. Law, and G. P. Asner (2004), Forest attributes from radar interferometric structure and its fusion with optical remote sensing, *BioScience*, 54(6), 561.
- Treuhaft, R. N., B. D. Chapman, J. R. dos Santos, F. G. Gonçalves, L. V. Dutra, P. M. L. A. Graça, and J. B. Drake (2009), The ambiguity in forest profiles and extinction estimated from multibaseline interferometric SAR, *Bol. Cienc. Geod.*, 15(3), 299.
- Turner, W., S. Spector, N. Gardiner, M. Fladeland, E. Sterling, and M. Steininger (2003), Remote sensing for biodiversity science and conservation, *Trends Ecol. Evol.*, 18(6), 306.
- Van Zyl, J. J., A. Chu, S. Hensley, Y. Lou, and Y. Kim (1997), The AIRSAR/TOPSAR integrated multifrequency polarimetric and interferometric SAR processor, *Conf. Publ. 449*, p. 100, Inst. of Electr. Eng., New York.
- Waring, R. H., and S. W. Running (1989), *Forest Ecosystems, Analysis at Multiple Scales*, Academic Press, San Diego, Calif.
- Wiens, J. A. (1989), *The Ecology of Bird Communities*, vol. 1, Cambridge Univ. Press, Cambridge, U. K.
-
- B. D. Chapman, Radar Science and Engineering, Jet Propulsion Laboratory, MS 300-319, Pasadena, CA 91109, USA. (bruce.chapman@jpl.nasa.gov)
- J. R. dos Santos, Divisão de Sensoriamento Remoto, Instituto Nacional de Pesquisas Espaciais, São José dos Campos, SP, Brazil. (jroberto@dsr.inpe.br)
- J. B. Drake, Forest Service, USDA, Tallahassee, FL 32303, USA. (jasondrake@fs.fed.us)
- L. V. Dutra, Divisão de Processamento de Imagens, Instituto Nacional de Pesquisas Espaciais, São José dos Campos, SP, Brazil. (dutra@dpi.inpe.br)
- F. G. Gonçalves, Department of Forest Ecosystems and Society, Oregon State University, Corvallis, OR 97331, USA. (Fabio.Goncalves@oregonstate.edu)
- P. M. L. A. Graça, Departamento de Ecologia, Instituto Nacional de Pesquisas da Amazônia, Manaus, AM, Brazil. (pmlag@inpa.gov.br)
- R. N. Treuhaft, Tracking Systems and Applications, Jet Propulsion Laboratory, MS 138-212, Pasadena, CA 91109, USA. (robert.treuhaft@jpl.nasa.gov)